



Catalytic Ru containing Pt₃Mn nanocrystals enclosed with high-indexed facets: Surface alloyed Ru makes Pt more active than Ru particles for ethylene glycol oxidation

Yao Wang^a, Meng Zheng^a, Hui Sun^a, Xin Zhang^{a,*}, Chenglong Luan^a, Yunrui Li^a, Liang Zhao^a, Huihui Zhao^a, Xiaoping Dai^a, Jin-Yu Ye^b, Hai Wang^c, Shi-Gang Sun^b

^a State Key Laboratory of Heavy Oil Processing, College of Chemical Engineering, China University of Petroleum, Beijing 102249, China

^b State Key Laboratory of Physical Chemistry of Solid Surfaces, Department of Chemistry, College of Chemistry and Chemical Engineering, Xiamen University, Xiamen 361005, China

^c National Institute of Metrology, Beijing 100013, China

ARTICLE INFO

Keywords:

Pt based alloy catalysts
High-indexed facets
Isolated Ru atoms
Interfacial effect
Ethylene glycol oxidation

ABSTRACT

Tuning the surface property of Pt based nanocrystals at the atomic level is of vital significance to meet superior electrocatalytic performance criteria. In this work, a new strategy to advance fundamental surface study on Pt based nanocrystals is addressed by implanting foreign metals as “active auxiliaries” onto the surface of Pt based nanocrystals to engineer a stable structured catalyst. Under the guidance of this concept, the Ru component was selected as “active auxiliary” to construct Ru containing Pt₃Mn catalysts by doping the isolated Ru atoms (Pt₃Mn–Ru) and Ru nanoparticles (Pt₃Mn@Ru) onto surface layer of Pt₃Mn concave nanocubes (CNCs). Strikingly, the Pt₃Mn–Ru CNCs showed the most optimal catalytic activity, durability and CO anti-poisoning ability toward ethylene glycol oxidation reaction (EGOR). The specific activity of Pt₃Mn–Ru CNCs is 1.32 mA cm^{−2}, which is 1.47 and 3.07 times higher than Pt₃Mn@Ru CNCs (0.90 mA cm^{−2}) and pure Pt₃Mn CNCs (0.43 mA cm^{−2}). The results of *in situ* Fourier transform infrared spectroscopy experiments revealed that Pt₃Mn–Ru CNCs were more in favor of C–C bond cleavage of EG and rapid oxidation/removal of intermediate poisonous CO_{ads}. Furthermore, the theoretical calculations revealed that the Pt₃Mn–Ru CNCs possessed a lower reaction barrier (1.69 eV) for oxidation of CO_{ads} assisted by adsorbed OH_{ads} species, and an energy-favorable position (2.88 Å) for reaction between CO_{ads} and OH_{ads}. This work disclosed a new tactics to develop a novel structured catalyst in possession of excellent electrocatalytic performance, which provided a promising methodology for designing Pt-based nanoparticles as efficient fuel cell catalysts.

1. Introduction

Polymer electrolyte membrane fuel cells (PEMFCs) as a promising candidate in closing the hydrogen energy cycles can directly convert the chemical energy of various small organic molecules (e.g. methanol, ethanol and ethylene glycol) into electrical energy accompanied with high energy conversion efficiency, low pollutant emission and high power density [1–7]. Today, Pt as an indisputably efficient catalyst is widely used due to its high intrinsic property [8,9]. However, the fundamental challenges at present for electrochemical oxidation of small organic molecules are ambiguous reaction mechanism, sluggish reaction kinetics, easy CO_{ads} poisoning and facile surface restructure catalysts [10–18]. Thus, how to fabricate a novel-structured Pt based catalysts possessing high electroactivity, great CO-resistance ability and

stable catalyst structure are the key for meeting the acquirement of large-scale application of PEMFCs.

In general, it is accepted that Pt based bimetallic nanocrystals enclosed by high-indexed facets (HIFs) are considered the promising catalysts in field of electrochemical reactions due to their high density of low-coordinated atoms [19–22]. However, after a certain number of electrochemical cycles, the higher surface energy and the easy-dissolution of transition metals are facile to accelerate surface Pt atoms with respect to migration and aggregation to each other [23–27]. This surface recession of Pt based catalysts could not meet the various requirements of industrial applications such as an initial high activity, a corresponding shape and performance stability during the lifetime of the catalyst.

Thus, extensive works had been made to resolve this shortcoming

* Corresponding author.

E-mail address: zhangxin@cup.edu.cn (X. Zhang).

<https://doi.org/10.1016/j.apcatb.2019.04.022>

Received 1 January 2019; Received in revised form 2 April 2019; Accepted 9 April 2019

Available online 11 April 2019

0926-3373/ © 2019 Published by Elsevier B.V.

and obtained significant progress. Li et al. reported Fe-doped Pt₃Ni nanocrystals that possess a stable initial octahedral shape after 16,000 potential cycles in acidic media while keeping about 75% of mass activity [28]. Zhang et al. used Cu component as foreign “active auxiliary” to engineer a Pt₂CuNi catalyst, which exhibited an enhanced activity and maintained a nearly initial shape after 4000 electrochemical cycles [29]. Huang and co-workers documented Mo-doped PtNi octahedral nanoparticles with an excellent ORR performance of 6.98 A mg_{Pt}⁻¹ [30]. Stress group discussed Rh-doped PtNi octahedral nanocatalysts with high activities up to 1.14 A mg_{Pt}⁻¹ combined with improved performance and shape stability [31]. Sun presented PtCu nanocrystals by trace Au and the mass activity loss of PtCuAu_{0.0005}/C was only 8%, much smaller than those of PtCu/C (32%), and Pt/C (52%) after 10,000 potential cycles [32]. In addition, non-metals as “active auxiliaries” introduced onto the surface layer of noble metal based nanoparticles were also reported. Chen et al. reported that the modified Pd/Ni nanoparticles by P possessed an improved electrocatalytic activity with 4.95 A per mg_{Pd}, which is 6.88 times that commercial Pt/C [33]. Wang and co-workers used P as “active auxiliary” to tune the electronic structure of Pt in PtNi-P catalyst, and this P doped PtNi nanocrystals showed about 2 times enhancement for ORR [34]. Moreover, the organic ligands (for example, N-containing polymers [35]) were also used as “active auxiliaries” to modify the chemical environment of Pt based nanoparticles and obtained enhanced electrocatalytic performance. However, the above impressive fruits are usually based on Pt based alloys with low-indexed facets (LIFs). Positive researches about improving the performance and stabilizing the surface structure covered with HIFs have been rarely reported [36]. Thus, developing a facilely efficient strategy to stabilize surface structure of Pt based catalysts covered by HIFs for meeting high activity and durability must be given priority.

It is known that the origin performance enhancement is deeply depended on the surface electronic and synergistic effects triggered by the local strain and ligand effect. Introducing other metals or nonmetals as “active auxiliaries” onto surface of Pt based nanocrystals bounded with HIFs is an efficient strategy for engineering/regulating surface structure and chemical environment of nanocrystals. The “active auxiliaries” could tune/modify the physicochemical properties of microcrystalline surface and possess Pt-based nanocrystals with improving catalytic reactive performance, as well as structure stability. Under the guidance of this concept, we have successfully implanted Mo component onto Pt based alloys covered by HIFs in forms of surface alloying and obtained excellent catalytic performance in our previous report [37]. However, another question that whether the larger size of “active auxiliary” has a better promoting effect on electrocatalytic reaction compared with surface alloying is still retained and ambiguous.

Herein, two types of Ru containing Pt₃Mn catalysts (Pt₃Mn–Ru CNCs and Pt₃Mn@Ru, the details see Section 2) are designed via regulating/fabricating the sizes of Ru component as illustrated in Fig. 1A. Afterwards, the experimental and theoretical technologies were carried out to explore the promoting effect of Pt₃Mn–Ru and Pt₃Mn@Ru catalysts towards ethylene glycol oxidation reaction (EGOR). Strikingly, in the process of electrocatalytic reaction, the Pt₃Mn–Ru catalyst shows an enhanced catalytic activity compared with the bare Pt₃Mn CNCs and commercial Pt/C. Meanwhile, the results of *in situ* Fourier transform infrared spectroscopy (FTIR) experiments reveal that Pt₃Mn–Ru is in favor of C–C bond cleavage of EG and rapid oxidation/removal of CO_{ads}. The theoretical calculations demonstrated that the Pt₃Mn CNCs modified by Ru atoms possess a lower reaction barrier for oxidation of CO_{ads}, and an energy-favorable position for reaction of CO_{ads} and OH_{ads}.

2. Experimental

2.1. Materials synthesis

2.1.1. Synthesis of Pt₃Mn alloy

220 mg polyvinyl pyrrolidone (PVP) and 88 mg glycine were put into 20 mL teflon-lined stainless-steel autoclave containing 1 mL hexachloroplatinic acid (H₂PtCl₆, 20 mM) aqueous solution and 4 mL manganese chloride (MnCl₂, 1.66 mM) aqueous solution and the mixture was sonicated and stirred at 30 °C for 5 min. Then, the resulting mixture was sealed and transferred into oven and heated at 200 °C for 7 h. Finally, the as-obtained resultant was washed and centrifuged by the mixture solution of water-ethanol (1:1) three times.

2.1.2. Synthesis of Pt₃Mn–Ru alloy

The Pt₃Mn–Ru alloy was fabricated based on the synthesis method of Pt₃Mn alloy with a slight modification. After reaction of 6 h of Pt₃Mn alloy, 180 µL RuCl₃ (2.5 mM aqueous solution) was injected into the above reaction solution and heated for another 2 h at 200 °C. Then the products were washed three times by the mixture solution of water–ethanol (1:1) and centrifuged thrice.

2.1.3. Synthesis of Pt₃Mn@Ru alloy

The well-defined Pt₃Mn alloys were separated from the reaction media and taken to re-disperse in 5 mL deionized water and then put into a 20 mL teflon-lined stainless-steel autoclave again. Then the 180 µL RuCl₃ (2.5 mM aqueous solution) and 38 mg ascorbic acid (AA) were injected into the mixed solution. The teflon-lined stainless-steel autoclave was put into the oven at 200 °C for 2 h before it was cooled to room temperature. Finally, the well-defined catalysts was washed and centrifuged thrice by water-ethanol (1:1) solution.

2.2. Electrochemical measurement

All of the electrochemical measurements were tested by three-electrode system on a CHI 760E electrochemistry workstation. The saturated calomel electrode (SCE) used as the reference electrode, a catalyst modified glassy carbon electrode (GCE, 3 mm in diameter) as the working electrode and the carbon rod as the counter electrode. We used the different aluminium oxide powder to polish the glassy carbon electrode before the experiments. After the electrode was dried, 6 µL catalyst inks were dropped onto GCE. Pt loadings were 4.40 µg, 4.82 µg and 4.56 µg for Pt₃Mn, Pt₃Mn–Ru and Pt₃Mn@Ru catalysts respectively, calculated by inductively coupled plasma-optical emission spectroscopy (ICP-OES). Thus, the loading per active surface area based on the Pt weight for Pt₃Mn, Pt₃Mn–Ru and Pt₃Mn@Ru catalysts is about 62.27, 68.22 and 65.54 µg cm⁻², respectively. Before electrochemical measurement, all electrodes were illuminated by UV-ozone (UVO) cleaning (10 W, with 185 nm and 254 nm emissions) for 12 h to remove the capping agents, which was confirmed as an efficient strategy and would hardly change the surface structure of nanocrystals by our previous studies [19,38]. Then 2 µL of 0.05 wt% nafion (Alfa Aesar) in ethanol was dropped on the electrode. We used the function “IR Comp Test Results” in electrochemical workstation to automatically obtain the values of solution resistance. In our measurements, the obtained values were about 10–15 Ω, and we used 80% of the values for IR correction.

EGOR was tested in a N₂-saturated 0.1 M HClO₄ and 0.5 M EG electrolyte at the range of 0.04–1.24 V (vs. RHE) with a sweep rate of 50 mV s⁻¹. The stability was tested by chronoamperometry at 0.7 V. For CO stripping measurement: the electrolyte was saturated with N₂ for 15 min. Afterwards the working electrode was immersed into the electrolyte under potential control at 0.05 V vs. RHE and the electrolyte was bubbled with nitrogen for additional 5 min. Then the gas was switched to CO and the bubbling occurs for another 15 min. And then the electrode was quickly moved to a fresh N₂-saturated solution, and the first two cycles were recorded at a scan rate of 50 mV s⁻¹ at room

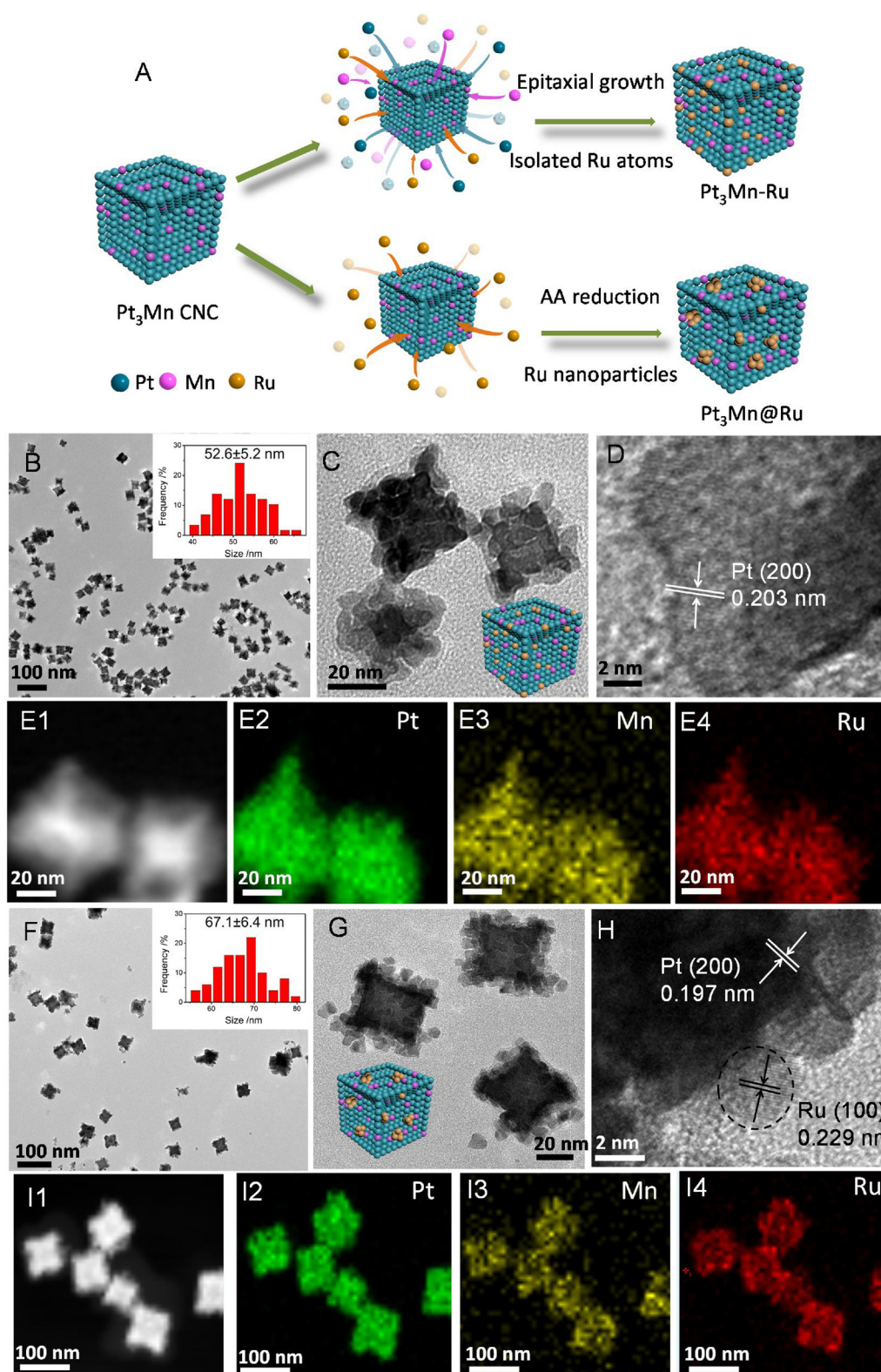


Fig. 1. (A) Illustration of the novel-structured Ru containing Pt₃Mn catalysts. (B) TEM and (C and D) HRTEM images, (E) HAADF-STEM image and the corresponding elemental mapping images of Pt₃Mn-Ru particles. (F) Typical TEM and (G and H) HRTEM images, (I) HAADF-STEM image and the corresponding elemental mapping images of Pt₃Mn@Ru particles.

temperature. The accelerated durability tests (ADTs) were performed at room temperature in 0.1 M HClO₄ + 0.5 M EG mixed solution by sweeping cyclic potential cycles between 0.04 and 1.24 V (vs. RHE) at a scan rate of 50 mV s⁻¹ for 1000 cycles.

2.3. DFT calculations

All the calculations were performed with the Dmol³ program in the Material Studio Package [39,40]. A Monkhorst-Pack mesh k-point set of 3 × 3 × 1 was adopted to sample the Brillouin zone. The generalized

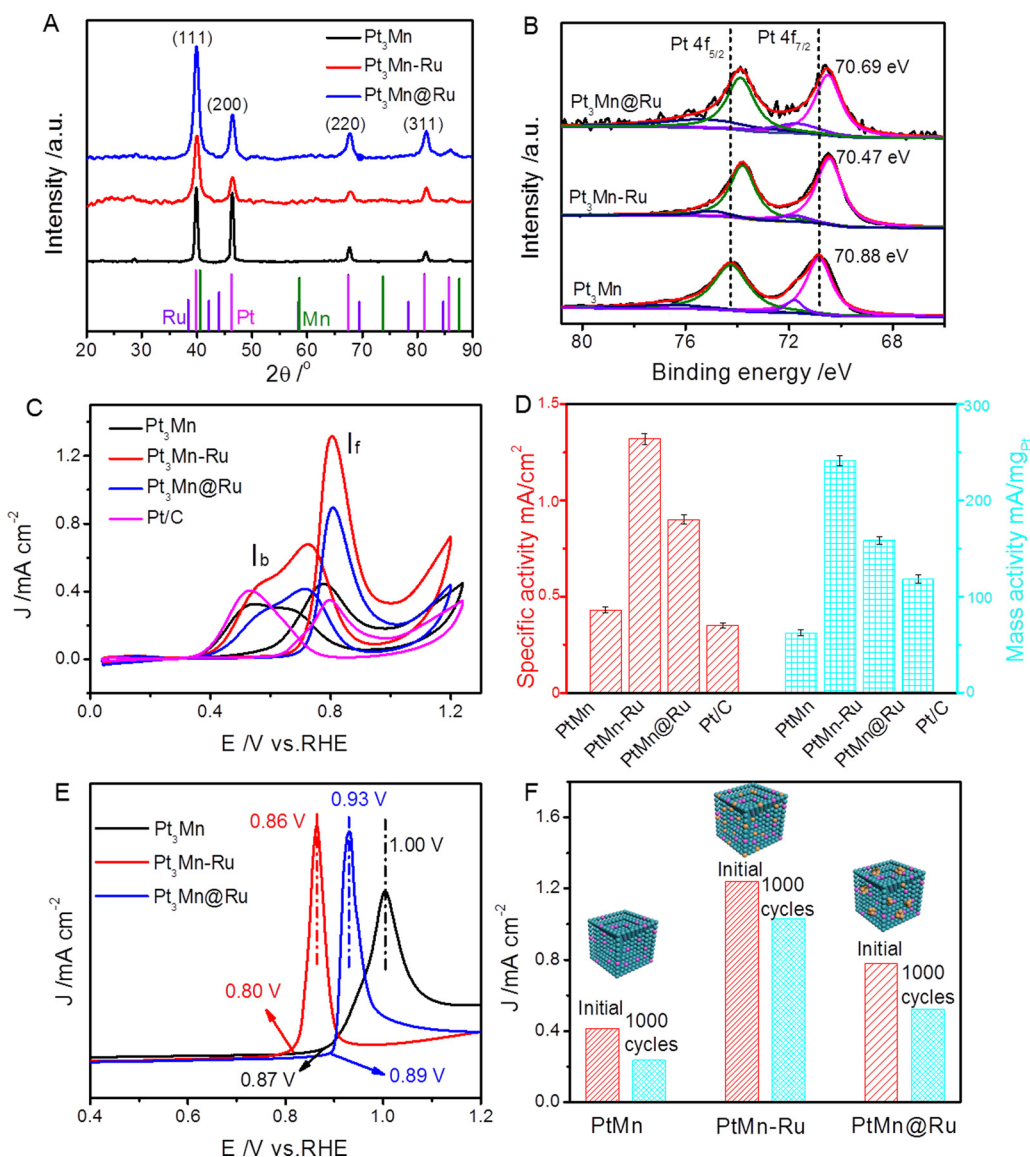


Fig. 2. (A) XRD patterns of Pt₃Mn, Pt₃Mn-Ru and Pt₃Mn@Ru catalysts. The vertical lines in green, pink and purple indicate the peak positions of the Mn (PDF card # 42-1120), Pt (PDF card # 04-0802) and Ru (PDF card # 06-0663) reflections, respectively. (B) XPS patterns of the Pt 4f of the as-prepared Pt₃Mn, Pt₃Mn-Ru and Pt₃Mn@Ru catalysts. (C) EGOR curves and (D) specific activity and mass activity of Pt₃Mn, Pt₃Mn-Ru, Pt₃Mn@Ru and commercial Pt/C catalysts in 0.1 M HClO₄ and 0.5 M EG solution at a sweep rate of 50 mV s⁻¹. (E) Cyclic voltammograms of CO stripping on Pt₃Mn, Pt₃Mn-Ru and Pt₃Mn@Ru catalysts in 0.1 M HClO₄ solution at a sweep rate of 50 mV s⁻¹. (F) The current densities of EGOR before and after 1000 cycles for three catalysts. (For interpretation of the references to color in this figure legend, the reader is referred to the web version of this article.)

gradient approach (GGA) [41] was used to all the atoms and PBE [42] was used as the exchange-correlation functional. Applied double numerical basis sets plus polarization functions (DNP) to represent atomic orbitals, and employed DFT semi-core pseudo-potentials (DSPPs) to treat metal core. Transition states were searched by linear synchronous transit (LST)/quadratic synchronous transit (QST) methods [43], and the transition states were proved by imaginary frequency.

The Pt (1 1 1) surface was built by periodically repeated four-layer slabs with (3 × 2) unit cells. The bottom two layers constrained to crystal lattice positions, and the rest layers were fully relaxed [32]. Ru₁/Pt was built with one Pt atom replaced by one Ru atom on the first layer, and Ru₈/Pt were modeled by and Ru₈ cluster adsorbed on Pt (1 1 1) surface, respectively. The adsorption energies of OH_{ads} were calculated according to the expression:

$$E_{\text{ads}} = E_{(\text{slab} + \text{molecule})} - E_{\text{slab}} - E_{\text{molecule, gas}} \quad (1)$$

where E_{ads} is the adsorption energy of OH_{ads}, $E_{(\text{slab} + \text{molecule})}$, E_{slab} , and $E_{\text{molecule, gas}}$ are the energies of OH adsorbed on the surface, the bare surface, and the gas-phase molecule, respectively. The reaction barrier of elementary steps was calculated based on the formula:

$$E_a = E_{\text{TS}} - E_R$$

where E_a is the reaction barrier of the elementary steps, E_{TS} and E_R are

the energies of transition states and products, respectively.

3. Results and discussion

3.1. Structural characterizations of catalysts

The Pt₃Mn CNCs were prepared according to our previous report [44], and the corresponding transmission electron microscopy (TEM) images are shown in Figs. S1–S3. The as-obtained Pt₃Mn particles yield above 95% selectivity of concave nanocubic structure and exhibit perfectly high-indexed facets. The lattice spacing is ca. 0.197 nm, which is the typical {200} lattice fringes of Pt.

The Ru modified Pt₃Mn CNCs were fabricated via hydrothermal strategy (illustrated in Fig. 1A), and the details were described in Section 2. The morphology and structure of the as-synthesized Pt₃Mn-Ru were characterized by TEM. Fig. 1B shows a typical TEM image of the uniform and monodispersed Pt₃Mn-Ru particles with an average diameter (apex-to-apex) of 52.6 ± 5.2 nm, and the yield of Pt₃Mn-Ru CNCs is above 96%. Observed by enlarged high resolution TEM (HRTEM, Fig. 1C), we can clearly see that, after adding Ru precursor, the surface restructure with a three dimensional gaps occurs on the Pt₃Mn CNCs, inferring that there is a surface evolution process during the regrowth of Pt₃Mn-Ru nanocrystals due to different atomic radius

and crystal cell parameters between Pt and Ru. The lattice spacing of well-defined Pt₃Mn–Ru nanocrystals is 2.03 Å in marginal domain, implying that Pt₃Mn–Ru nanocrystals are still enclosed by {200} facets, clearly demonstrated by the HRTEM image in Figs. 1D and S4, which is nearly close to pure Pt₃Mn CNCs. The slightly enlarged lattice spacing compared with pure Pt₃Mn (1.97 Å) nanocrystals indicates that Ru atoms are successfully implanted onto the surface lattice of Pt₃Mn particles. The element distributions of the obtained Pt₃Mn–Ru nanocrystals are analyzed by high-angle annular dark-field scanning transmission electron microscopy (HAADF-STEM) energy-dispersive X-ray elemental mapping (Fig. 1E). The Pt, Mn and Ru elements are uniformly distributed throughout these particles, which confirms that the Ru component is homogeneous implanted into Pt₃Mn particles. The content of Pt:Mn:Ru determined by ICP-OES (Table S1) was about 74.1:24.2:1.7.

The Pt₃Mn@Ru nanoparticles are obtained via reducing Ru precursor under the presence of AA and characterized by typical TEM. Observed from Fig. 1F, the Pt₃Mn@Ru particles are uniformly dispersed with an average size (apex-to-apex) of 67.1 ± 6.4 nm. It is observed that many tiny particles with a size of 2–5 nm are supported on Pt₃Mn surface, which can be clearly reflected in Fig. 1G. The HRTEM image (Figs. 1H and S5) reveals that the lattice fringes of tiny particles are approximately 2.3 Å, which is in consistence with the {100} facet of the Ru⁰ crystal (PDF#06-0663). The elemental mapping (Fig. 1I) exhibits Ru enrichment in surface layer demonstrating Ru nanoparticles successfully supported on the surface of Pt₃Mn CNCs. The ICP-OES results (Table S1) demonstrate that the ratios of Pt:Mn:Ru is about 76.3:22.2:1.5.

XRD patterns of Pt₃Mn, Pt₃Mn–Ru and Pt₃Mn@Ru catalysts are exhibited in Fig. 2A, which all exhibits a similar single *fcc* phase. The diffraction peaks centered at ca. 39°, 46°, 67° and 81° are nearly close to typical crystalline orientations of (111), (200), (220) and (311) of Pt phase. Noting that no typical diffraction peaks of Ru or its oxides phase was detected in XRD patterns of Pt₃Mn–Ru and Pt₃Mn@Ru catalysts because the low amount of Ru is below the detection limit of XRD apparatus. Clearly, observed from the enlarged local peaks of XRD patterns in Fig. S6, the peak positions of Pt₃Mn–Ru catalysts has a slightly positive shift (0.38° for Pt₃Mn–Ru), while the Pt₃Mn@Ru exhibits same positions for diffraction signals compared with bare Pt₃Mn catalyst. On the basis of Bragg's equation ($2d \sin \theta = n\lambda$) and the equation $d_{hkl} = a/(h^2 + k^2 + l^2)^{1/2}$ of the *fcc* structure, the cell constant *a* of the Pt₃Mn–Ru and Pt₃Mn@Ru catalysts are calculated to be ca. 3.78 Å and 3.90 Å, respectively, which are smaller than bulk Pt (3.92 Å). According to the XRD patterns and the Debye–Scherrer equation [45,46] (Table 1), Ru entering the Pt₃Mn lattice can induce lattice contraction and strain variation, and the strain variation of Pt₃Mn–Ru (3.75%) nanoalloys is higher than that of Pt₃Mn (0.51%), which would enhance catalytic performance of nanocrystals.

X-ray photoelectron spectroscopy (XPS) was carried out to investigate the chemical states of Ru modified Pt₃Mn alloys. Fig. S7 shows all element signals of XPS spectra of Pt₃Mn, Pt₃Mn–Ru and Pt₃Mn@Ru catalysts. As shown in Fig. 2B, the XPS spectrum signals of Pt in these three catalysts can be decomposed into two groups of peaks: metallic state (Pt⁰) and oxidized state (Pt^{II}). And we find that the metallic state of Pt is the dominate species in catalyst surface. In terms of Pt₃Mn CNC

spectrum, the metallic state of Pt centered at 70.88 eV, which has a negative shift of ca. 0.02 eV compared with pure metallic Pt (Pt 4f_{7/2}: 70.90 eV), referring electron donation from Mn to Pt. The oxidized state of Pt located at 71.80 eV is probably originates from the passivated Pt–O layer [47]. The signals of Pt 4f_{7/2} in Pt₃Mn–Ru and Pt₃Mn@Ru catalysts are about 70.47 and 70.69 eV, with a negative shifts of approximately 0.43 and 0.21 eV compared with Pt₃Mn CNCs (4f_{7/2}: 70.88 eV). This result indicates that after the decoration of Ru, the electrons transfer from Ru to Pt, following strengthen the electronic density of Pt, which is in favor of boosting the catalytic activity [48–50]. Simultaneously, there are a small quantity of oxidized state of Pt in the surface of Pt₃Mn–Ru and Pt₃Mn@Ru catalysts, which are also attributed to surface passivation. However, it is difficult to distinguish the peaks of Ru 3d and C 1s (Fig. S8) because the Ru 3d peak is close to C 1s peak, and the content of Ru is rather low (1.7% for Pt₃Mn–Ru, 1.5% for Pt₃Mn@Ru).

3.2. Electrochemical EGOR performance of catalysts

To gain comprehensive insights into the surface structure–performance relationship of the Ru modified Pt₃Mn towards EGOR. The EGOR measurements of Pt₃Mn, Pt₃Mn–Ru, Pt₃Mn@Ru and commercial Pt/C catalysts were carried out in the 0.1 M HClO₄ and 0.5 M EG electrolyte. All the electrochemical active surface area (ECSA) values were calculated based on the hydrogen desorption domains, as expounded in Figs. S9 and S10. Before the electrochemical measurement, these catalysts were cleaned by UVO. Herein, we used pure Pt nanocrystals as model catalyst to demonstrate the promoting impact of UVO treatment (Fig. S11). As shown in Fig. S12, The ECSAs of Pt nanoparticles with UVP treatment shows a higher value ($9.91 \text{ m}^2 \text{ g}_{\text{Pt}}^{-1}$) than pure Pt without UVO treatment ($3.58 \text{ m}^2 \text{ g}_{\text{Pt}}^{-1}$), proving that capping agents can be effectively removed from the nanoparticle. Meanwhile, FT-IR spectra (Fig. S13) was used to analyze the surface environment of Pt nanocrystals. It is obviously seen that the treated Pt particles shows weak absorption bands in the range of 2000–1200 cm^{−1} and 3060–2750 cm^{−1}, indicating that capping agents can be mostly removed from the nanocrystal surfaces by UVO cleaning. Thus, on the basis of ECSA values and FT-IR results, it can be concluded that UVO treatment is an efficient method for cleaning surface of nanocrystals.

The ECSA values (Table S2) of Pt₃Mn–Ru and Pt₃Mn@Ru are 18.3 and $17.6 \text{ m}^2 \text{ g}_{\text{Pt}}^{-1}$, respectively, which are 1.26 and 1.21 times higher than pure Pt₃Mn particles ($14.5 \text{ m}^2 \text{ g}_{\text{Pt}}^{-1}$), indicating that the Ru decorated Pt₃Mn particles show an enhanced intrinsic activity of Pt. Fig. 2C shows the EGOR performance curves of these catalysts. The specific activities of Pt₃Mn–Ru and Pt₃Mn@Ru are 1.32 and 0.90 mA cm^{-2} , which are 3.07 and 2.09 times higher than that of pure Pt₃Mn (0.43 mA cm^{-2}) catalysts, respectively. The mass activities (Fig. 2D) of Pt₃Mn–Ru and Pt₃Mn@Ru are 241.6 and $158.4 \text{ mA mg}_{\text{Pt}}^{-1}$, which are 3.87 and 2.54 times higher than that of pure Pt₃Mn ($62.3 \text{ mA mg}_{\text{Pt}}^{-1}$) catalysts, respectively. These above results demonstrate that surface alloyed Ru implanted in Pt₃Mn lattice are more in favor of improving the electrocatalytic performance of EG. These results also mean that not all surface Pt atoms are catalytically equivalent because of the heterogeneity in the surface of Ru decorated Pt₃Mn catalyst. Simultaneously, the Pt₃Mn–Ru catalyst shows 3.77 times specific activity and 2.05 times mass activity higher than that of commercial Pt/C (specific activity: 0.35 mA cm^{-2} , mass activity: $118 \text{ mA mg}_{\text{Pt}}^{-1}$). We attribute this to three aspects: (i) the surface alloyed Ru could modify/optimize the surface electronic structure at the greatest extent, which can tune the adsorption/desorption capacities of activating reactant molecules or intermediates and boost the catalytic reactions [51–53]. (ii) Compressive strain triggered by incorporation of Ru is in favor of the enhancement of electrocatalytic performance [54–57]. (iii) Synergistic effect between Pt and Ru surface atoms are favor the removal of poisoning intermediates (mainly CO_{ads}), due to the stronger oxophilic effect of Ru, which can accelerate the oxidation/desorption of CO_{ads} via L–H mechanism

Table 1
The X-ray diffraction (XRD) results of different samples.

Samples	2θ/degree (200)	Lattice parameter (Å)	Strain (%)
Pt crystal (JCPDS-04-0802)	46.24	0.392	–
Pt ₃ Mn	46.41	0.390	0.51%
Pt ₃ Mn–Ru	46.79	0.378	3.57%
Pt ₃ Mn@Ru	46.42	0.390	0.51%

proved by DFT calculations thereafter discussed [30,58–60]. We also conducted CO-stripping experiments to determine the ECSA values and EGOR performance based on CO oxidation peak, as shown in Table S2. The resulting ratios of ECSA_H:ECSA_{CO} are 1.00:1.15, 1.00:1.21 and 1.00:1.16 for Pt₃Mn, Pt₃Mn–Ru and Pt₃Mn@Ru catalysts, respectively, which are in agreement with that of typical Pt materials [61].

As we all know, during the process of alcohol electro-oxidation reaction, CO-poisoning on the Pt active sites is inevitable, so how to remove the negative effect of CO intermediate products on Pt based catalysts is crucial for further study. It is demonstrated [62–64] that Ru component can affect the adsorption energy of an adsorbed substrate such as CO_{ads} on the bimetallic surface by the direct electronic coupling between different domains. Seen from Fig. 2C, the I_f/I_b (where I_f is the forward current density and I_b is the backward current density) values of Pt₃Mn, Pt₃Mn–Ru, Pt₃Mn@Ru and commercial Pt/C catalysts are 1.30, 1.94, 1.93 and 0.85, respectively, which reveals that the EG will be more effectively oxidized on the isolated Ru atoms modified Pt₃Mn surface, producing less CO_{ads} poisoning species, thereby possessing higher CO-assistance ability [65,66]. The CO stripping experiments are also employed to further verify high CO-resistant activity of isolated Ru atoms modified Pt₃Mn particles, as shown in Fig. 2E. The onset potential of Pt₃Mn–Ru is 0.80 V, lower than that of Pt₃Mn@Ru (0.89 V) and Pt₃Mn (0.87 V) catalysts, indicating CO_{ads} oxidation/desorption is allowed occurred at low potential on the surface of Pt₃Mn–Ru catalyst.

The accelerated durability tests (ADTs) were performed to evaluate the catalytic stability of Pt₃Mn, Pt₃Mn–Ru and Pt₃Mn@Ru catalysts. Fig. S14 show the various curves towards EGOR for Pt₃Mn, Pt₃Mn–Ru and Pt₃Mn@Ru catalysts before and after 1000 cycles, and the corresponding values of current density of three catalysts as shown in Fig. 2F. It is obviously observed that the Pt₃Mn catalyst shows a drastic performance decline compared with Pt₃Mn–Ru and Pt₃Mn@Ru catalysts, revealing a promoting effect of Ru component on keeping initial activity. In general, the activity degradation of Pt₃Mn, Pt₃Mn–Ru and Pt₃Mn@Ru are approximately 46.0%, 16.8% and 33.1%, respectively, indicating that surface alloyed Ru in surface lattice of Pt₃Mn CNCs has an optimized promoting effect on EGOR. Their stability towards EGOR was also assessed by applying the chronoamperometric measurements, as shown in Fig. S15. The Pt₃Mn–Ru and Pt₃Mn@Ru catalysts show the slow current decay in comparison with bare Pt₃Mn catalyst. It also should be pointed out that the performance of Pt₃Mn–Ru for EGOR is superior than previously reported Pt based catalysts (Table S3), such as PtNi_{0.67}Pd_{0.26} NWs/C [67], Pt_{4.5}Pd NWs [68], PtPd@Pt nanocrystals/rGO [69]. Furthermore, the Pt₃Mn–Ru catalyst exhibits a better structural stability compared with bare Pt₃Mn catalyst. On the other hand, the isolated Ru atoms implanted in crystal surface of Pt is more making for higher activity than Ru particles.

In addition, the Pt@Ru CNCs were also prepared under the same experimental conditions. As shown in Fig. S16, it can be obviously seen that Ru containing Pt CNCs (donated as Pt@Ru CNCs) was successfully synthesized with Ru particle sizes being several nanometers. And the corresponding catalytic performance of Pt@Ru CNCs is also tested. Fig. S17A shows the typical cyclic voltammetric curves in 0.1 M HClO₄ solution. The ECSA value of Pt@Ru CNCs is 16.8 m² mg^{−1}, lower than these of Pt₃Mn–Ru and Pt₃Mn@Ru catalysts, indicating that three component surface possesses a higher electronic coupling effect. The EGOR was also performed in 0.1 M HClO₄ and 0.5 EG solution. As shown in Fig. S17B, the specific activity of Pt@Ru CNCs is 0.78 mA cm^{−2}, lower than these of Pt₃Mn–Ru and Pt₃Mn@Ru catalysts. Meanwhile, its stability towards EGOR was also assessed by applying the chronoamperometric measurements, as shown in Fig. S17C. On the other hand, after testing 1000 cycles of EGOR (Fig. S17D), the activity degradation of Pt@Ru CNCs is approximately 22%, lower than Pt₃Mn–Ru CNCs, unravelling that surface alloyed Pt–Mn–Ru is in favor of oxidation of EG.

The Pt₃Ru particles were prepared with the feeding ratio (Pt:Ru) of 3:1 under the same conditions with pure Pt₃Mn CNCs. As shown in Fig.

S18, it can be obviously observed that the morphology of Pt₃Ru nanoparticles is predominately irregular polygons with particle size being about 20 ± 5 nm. The lattice distance is about 0.225 nm, in nearly consistence with typical Pt (1 1 1) plane. The performance of Pt₃Ru nanoparticles towards EGOR is exhibited as shown in Fig. S19. The ECSA value obtained from CV curve (Fig. S19A) is about 11.2 m² g_{Pt}^{−1}, lower than Ru containing Pt₃Mn CNCs, demonstrating that Pt based alloys enclosed HIFs possess amounts of active sites. The specific activity (Fig. S19B) of Pt₃Ru nanoparticles is about 0.65 mA cm^{−2}, lower than Ru containing Pt₃Mn CNCs. In addition, the stability of Pt₃Ru nanoparticles was also evaluated by applying the chronoamperometric measurements, as shown in Fig. S19C. Furthermore, after testing 1000 cycles of EGOR, the activity degradation of Pt₃Ru CNCs is approximately 34% (Fig. S19D), lower than Ru containing Pt₃Mn CNCs, revealing that Ru modified Pt₃Mn–Ru CNCs possess a stable structure.

After the durability test, the catalyst powders were collected and dried for further characterizations. As shown in Fig. S20, it is clearly noted that the edges and corners of Pt₃Mn CNCs became disappear after stability testment, while the Pt₃Mn–Ru could nearly keep its initial intact. Simultaneously, ICP-OES was used to quantitative analyze the elementary composition of PtMn, Pt₃Mn–Ru and Pt₃Mn@Ru catalysts after 1000 cycles. Observed from Table S1, after the stability tests, the composition ratio of Pt:Mn in Pt₃Mn CNCs was approximately 79.2:21.8, lower than initial state (Pt:Mn = 71:29), indicating that Mn located in the catalyst near-surface dissolved in the electrolyte. While, in terms of Ru containing Pt₃Mn alloys, the ratios of Pt:Mn:Ru in Pt₃Mn–Ru and Pt₃Mn@Ru CNCs are about 75.1:23.4:1.5 and 77.9:20.9:1.2, in good accordance with the initial state. As a conclusion, Ru containing Pt₃Mn CNCs possess a more stable surface structure compared with bare Pt₃Mn CNCs.

3.3. In situ FTIR spectroscopy measurements of catalysts

In situ FTIR spectroscopy was carried out to further determine the structure-performance relationship between superior EGOR and modified Pt₃Mn surface triggered by isolated Ru atoms, since this technique is sensitive to the chemical identity of significant intermediates and products at the catalyst surface as the reaction proceeds. It is generally accepted that EGOR followed a so-called dual-pathway mechanism [70–72], namely C1–C2 pathways, due to EG being a typical small organic molecule with a C–C bond, resulting in a series of complex reaction product, involving adsorbed intermediates, side reactions, products, and byproducts [73–75]. According to some previous reports [70–72], the simplified reaction pathways of EGOR on Pt based catalysts are illustrated in Fig. S21. The oxidation of EG will go through two different pathways based on whether the bond breaks or not. The complete oxidation products are mainly C1 organic intermediate species (COH_x), and further oxidized to CO_L, finally forming CO₂. The incomplete oxidation is mainly the oxidation of hydroxyl groups, keeping the C–C bond intact. Then the C2 species are further oxidized to C1 species via breaking C–C bond, and then follow the complete oxidation pathway. The essential nature of C1-pathway and C2-pathway is that the C–C bond cleavage of EG will occurred or not. The complete oxidation of EG, namely C1-pathway, is preferred to harvest the higher energy density. Thus, in situ FTIR spectrums of pure Pt₃Mn, Pt₃Mn–Ru and Pt₃Mn@Ru catalysts were performed in 0.1 M HClO₄ and 0.5 M EG solution as shown in Fig. 3A–C, respectively. The negatively obvious band near 2343 cm^{−1} is due to CO₂ formation [76,77] (Table 2). According to previous reports, two strong downward IR bands at 1076 and 1107 cm^{−1} can be attributed to the C–O stretching vibration of C₂ immediate product from the incomplete oxidation of EG [78–83]. Two slight IR bands at 1402 and 1472 cm^{−1} belong to the symmetric stretch of COO[−] in glycolate ions [81,82]. Observed clearly from Fig. 3D–F, the weakest IR band intensity of C₂ immediate product (glyoxylate, glyoxal, glycolate) on Pt₃Mn–Ru surface indicates that the great C–C bond cleavage ability, which causes generating a large

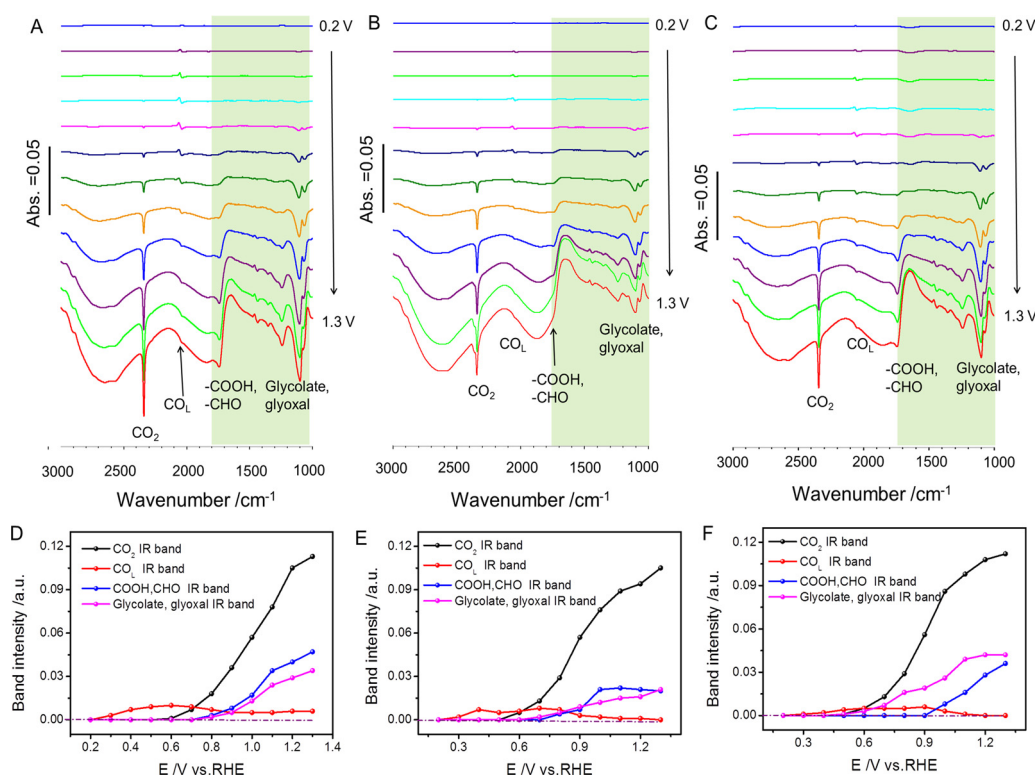


Fig. 3. In situ FTIR spectra for EGOR on (A) Pt₃Mn and (B) Pt₃Mn–Ru, (C) Pt₃Mn@Ru catalysts in 0.1 M HClO₄ + 0.5 M EG solution, tested potential: from 0.2 V to 1.3 V vs. RHE. Band intensity of different generated species for (D) Pt₃Mn, (E) Pt₃Mn–Ru, (F) Pt₃Mn@Ru catalysts at different reaction potential.

Table 2

Peak assignments for the infrared spectra of EGOR on Pt based catalysts in acidic media.

Wavenumber/cm ^{−1}	Functional group or chemical species
2983, 2906	C–H stretching in CH ₃ ,CH ₂ [77]
2632 (broad)	O–H stretching in COOH [77]
2343	Asymmetric CO ₂ stretch [75,76]
2050	Linearly bonded CO [72–74]
1713	C=O stretching, carbonyl in COOH or CHO [77]
1620	C=O of adsorbed 2-hydroxyacetyl [78,79]
1402, 1472	Symmetric stretch of COO [−] in glycolate [80,81]
1361	Glycolate, HCO ₃ [−] [75,82]
1236	C–O stretch of glycolate [79]
1107	Typical peak for glyoxylate [80]
1076	Aldehyde stretch (glyoxal, glycolate) [72–80]

amount of CO₂ at potential range of 0.6–1.2 V (vs. RHE).

It is noteworthy that CO intermediate species (linearly bonded CO) can be clearly observed at around 2050 cm^{−1}. The band intensity of CO_L is dependent dominantly on the potential, resulting from the “stark effect” [80]. With the increase of potential (Fig. 3D–F), the band intensity of CO_L increases at first and then diminishes at high potential. The above results demonstrate that C–C bond cleavage rate of EG is slower than CO_L oxidation at high potential. Observed from the curves of CO₂ band intensity, we can obviously see that the onset potential of CO₂ generation on Pt₃Mn–Ru (0.45 V) surface is lower than Pt₃Mn (0.6 V) and Pt₃Mn@Ru (0.5 V) surface, and the accumulation of CO₂ on Pt₃Mn–Ru surface is larger than other catalysts, implying that the Pt₃Mn surface modified by isolated Ru atoms has a benefit on rapid oxidation/removal of CO_L to CO₂.

Adsorption/oxidation transients of intermediate species were recorded at a given constant potentials (0.5 V vs. RHE), as shown in Fig. S22. There are two rapidly growing bands at ca. 2343 and 2050 cm^{−1}, which belonged to CO₂ and CO_L, respectively. The band at 2050 cm^{−1} broadens with the increase of time, indicating that CO_L amount

increases as the reaction goes on, and also implying that the faster C–C bond breaking rate than CO_L oxidation/desorption rate at 0.5 V (vs. RHE). Compared with the bare Pt₃Mn and Pt₃Mn@Ru catalysts, the Pt₃Mn–Ru shows a weaker CO_L bands intensity and stronger CO₂ bands intensity, demonstrating that the Pt₃Mn–Ru surface is more in favor of oxidation/desorption of CO_L.

On the basis of in situ FTIR results, the different reaction pathway (C1 pathway and C2 pathway) of EGOR on Ru containing Pt₃Mn catalyst is illustrated in Fig. 4. It can be found that the ratio C2/C1 intermediate species (C2 species: glycolaldehyde, glyoxal, glycolic acid, glyoxylic acid, oxalic acid; C1 species: formaldehyde, formic acid, CO, CO₂) on Pt₃Mn–Ru CNCs decreased, indicating Pt₃Mn–Ru CNCs are in favor of C–C bond cleavage of EG and obey the complete oxidation pathway. Furthermore, the weaker CO_L signal on Pt₃Mn–Ru CNCs demonstrated that Pt₃Mn–Ru CNCs are in favor of rapid oxidation/removal of intermediate poisonous CO_{ads}.

To the best of our knowledge, the possible CO poisoning route on the Pt site is mentioned: the Pt atom site catalyzes oxidation of an alcohol molecule to form strong adsorbed CO_{ads}, which can only be further oxidized to CO₂ at large overpotentials [70,84–87]. In this work, the Ru containing Pt₃Mn catalysts show a higher CO_{ads}-resistance ability compared with bare Pt₃Mn. It is generally reported that [60,85] Ru alloying with Pt could enhance the CO_{ads} durability in site-poisoning from ligand effect (electronic effect) and synergistic effect (bifunctional effect). In terms of electronic effect, introduction of Ru component into surface could change the electronic structure of Pt, optimize the d-center bond position of Pt and thus weaken the adsorption energy of CO_{ads} on the Pt active sites, followed by releasing more sites to adsorb another methanol molecule [62]. According to the bi-functional effect [60,88] (illustrated in Fig. S23), Ru can activates and breaks H₂O molecule and adsorbs OH_{ads} species at ca. 0.2–0.3 V (R1), lower in comparison with Pt. Simultaneously, the intermediate CO_{ads} adsorbed on the Pt sites then reacts with OH_{ads} through a Langmuir–Hinshelwood (L–H) mechanism, generating CO₂ and concomitantly liberating the metal atoms for further adsorption (R2).

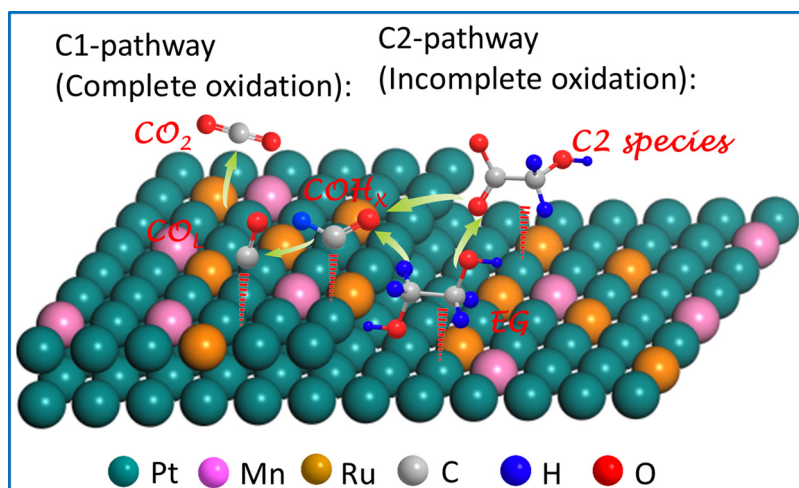
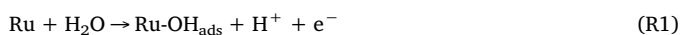


Fig. 4. Reaction pathways for interfacial reaction of EG at the Pt electrode.



3.4. DFT calculations

Herein, it is noted that two-type of Ru modified Pt₃Mn catalysts showed different CO poison resistance towards EGOR, which was exclusively attributed to the surface structure of Ru containing Pt₃Mn. Thus, in order to further make clear the influence of surface alloyed Ru and nanosized Ru particles on CO_{ads} oxidation, the theoretical calculations were carried out for further elaboration. To be specific, a single Ru atom implanted on Pt (1 1 1) crystal (Ru₁@Pt plane) is built and stands for alloyed Pt₃Mn–Ru surface, whereas the Ru nanoparticles involving eight Ru atoms supported on Pt (1 1 1) crystal (Ru₈@Pt plane) is also modeled to represent Pt₃Mn@Ru surface (Fig. S24). On the basis of DFT calculation results, the advantages for CO_{ads} oxidation improvement of surface alloyed Pt–Mn–Ru particles can be ascribed to three respects:

First, the reaction energies of CO_{ads} oxidation via L–H mechanism on Ru₁@Pt plane and Ru₈@Pt plane were calculated. As shown in Fig. 5A, the energy barrier for bond-breaking of O–H in adsorbed OH_{ads} is about 1.69 eV on Ru₁@Pt plane, while it is 1.99 eV on Ru₈@Pt plane. The energy barrier decreases by 0.30 eV, indicating the surface alloying is more favor of oxidation/removal of CO_{ads}.

Second, the promoting effect of Ru component is attributed to the adsorption/desorption of OH species, so the higher adsorption energy is detrimental for next reaction towards oxidation of CO_{ads}. As shown in Fig. 5B and C, the adsorption energy of OH_{ads} on Ru₈@Pt plane is 3.77 eV, higher than that on Ru₁@Pt plane (2.81 eV), which goes against the further combination with CO_{ads}. In addition, compared with pure Pt (the adsorption energy of OH_{ads} is about 2.19 eV, Fig. S25), demonstrating that Ru is more active than Pt in water-discharge reaction and adsorption of OH (R1), in consistence with previous reports [60].

Third, it is reported [63] that only the distance between Pt–CO_{ads} and Ru–OH_{ads} species is less than 4.0 Å, the oxidation reaction of CO_{ads} (R2) with OH_{ads} could occur. In our system (Fig. 5D and E), the distance of adsorbates (CO_{ads} and OH_{ads}) siting at nearest positions on Ru₁@Pt plane is about 2.88 Å, which is energy-favorable for reaction of CO_{ads} and OH_{ads}. The distance of adsorbates on Ru₈@Pt plane is about 3.94 Å, which is the critical position available for the reaction. Thus, it can be further referred that when Ru nanoparticles became larger, the distance of OH_{ads} adsorbed on the upside of Ru particles is far away from the nearest CO_{ads}, so these adsorbed OH_{ads} are not helpful to oxidation/

removal of CO_{ads}. Therefore, the surface alloying of Pt–Ru is the optimal reaction site for oxidation/removal of CO_{ads} compared with Ru particles supported on Pt surface.

Thus, from the viewpoints of experimental and theoretical results, the improved electrocatalytic performance of the Pt₃Mn–Ru catalysts are mainly attributed to the four aspects: (i) the unique surface nanostructure Pt₃Mn–Ru enclosed with HIFs, can offer abundant defects, such as, lattice disorder, gap atoms, and amounts of high density of undercoordinated Pt atoms (steps, kinks and edges), which benefit the higher catalytic performance [89,21,90–92]; (ii) Mn and Ru could modify/optimize the surface electronic structure and downshifts the *d*-band center of Pt through ligand effect, which can tune the adsorption/desorption capacities of activating reactant molecules or intermediates and boost the catalytic reactions [51–53]; (iii) strain effect triggered by incorporation of Ru can result in lattice mismatch and *d*-band center downshifts, which are also benefit to high catalytic performance [54–57]; (iv) synergistic effect between Pt and Ru surface atoms are favor the removal of poisoning intermediates (mainly CO_{ads}), due to the stronger oxophilic effect of Ru, which can accelerate the oxidation/desorption of CO_{ads} via L–H mechanism [30,58–60].

4. Conclusion

In summary, a stable novel-structured catalyst was fabricated via engineering foreign metals or nonmetals as “active auxiliaries” onto the surface of Pt based nanocrystals bounded with HIFs. Then the isolated Ru atoms (Pt₃Mn–Ru) and Ru nanoparticles (Pt₃Mn@Ru) doped onto Pt₃Mn catalysts were engineered via wet-chemical method. We find that Pt₃Mn–Ru catalyst exhibits superior electrocatalytic activity, durability and CO-resistance ability in the process of EGOR under the electronic and synergistic effect. The specific activity of Pt₃Mn–Ru is 1.32 mA cm^{−2}, which is 1.47 and 3.07 times higher than Pt₃Mn@Ru CNCs (0.90 mA cm^{−2}) and pure Pt₃Mn CNCs (0.43 mA cm^{−2}). The results of in situ FTIR experiments demonstrate that Pt₃Mn–Ru catalyst is in favor of C–C bond cleavage of EG and rapid oxidation/removal of CO_{ads}. The DFT calculations demonstrated that the Pt₃Mn–Ru CNCs possessed a lower reaction barrier (1.69 eV) for oxidation of CO_{ads} assisted by adsorbed OH_{ads}, and an energy-favorable position (2.88 Å) for reaction between CO_{ads} and OH_{ads}. This work provides an efficient method for improving electrocatalytic performance of Pt based catalysts via surface engineering strategy.

Conflicts of interest

The authors declare no competing financial interest.

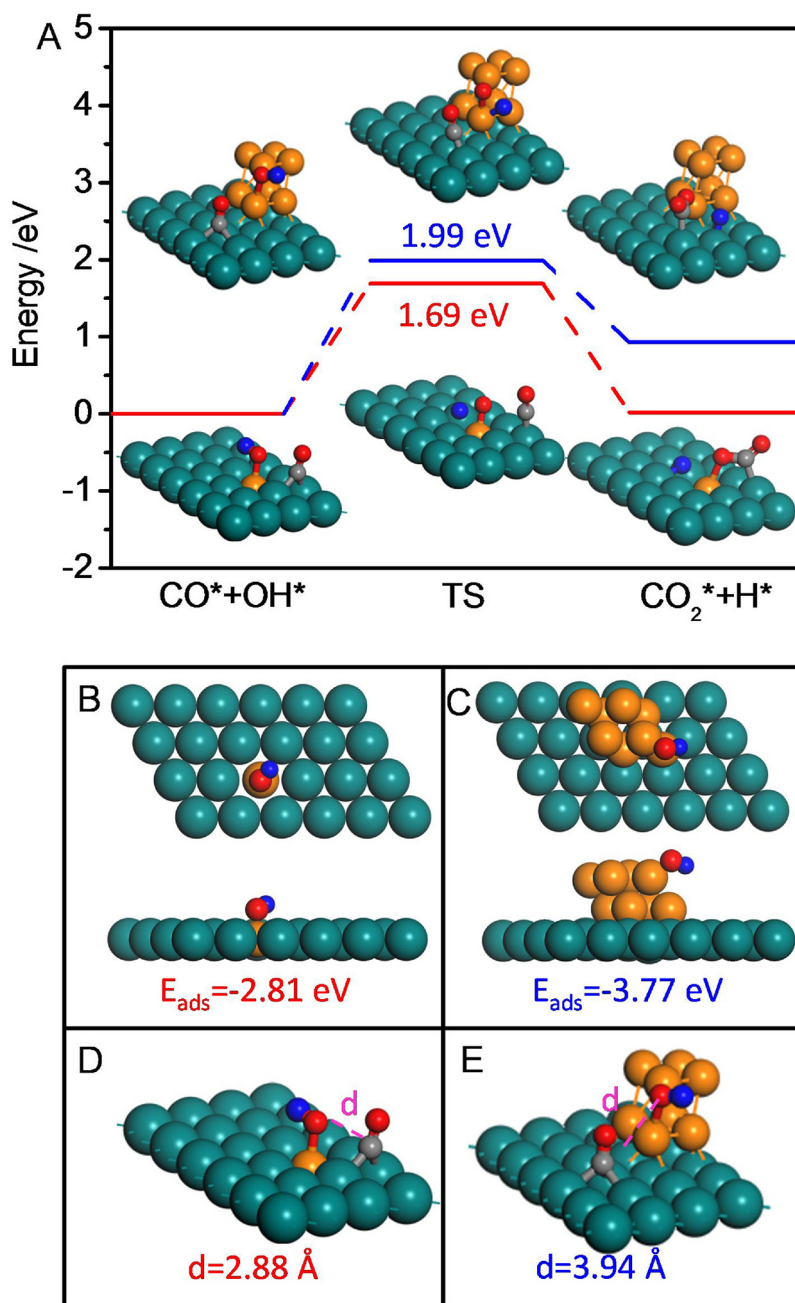


Fig. 5. A representative reaction states of the molecular dynamic process with adsorbates siting at nearest energy-favorable positions. (A) Reaction energy diagram of CO_{ads} oxidation via L–H mechanism on $\text{Ru}_1\text{@Pt}$ plane and $\text{Ru}_8\text{@Pt}$ plane. The binding energies of adsorbed OH on (B) $\text{Ru}_1\text{@Pt}$ plane and (C) $\text{Ru}_8\text{@Pt}$ plane. The distance of adsorbates (CO_{ads} and OH_{ads}) siting at nearest energy-favorable positions on (D) $\text{Ru}_1\text{@Pt}$ plane and (E) $\text{Ru}_8\text{@Pt}$ plane.

Acknowledgments

The authors acknowledge the financial supports from the NSFC (Nos. 21573286, 21173269, 21576288, U1662104), Specialized Research Fund for the Doctoral Program of Higher Education (20130007110003) and Ministry of Science and Technology of China (No. 2015AA034603), Science Foundation of China University of Petroleum, Beijing (No. 2462015YQ0304) and the open fund of State Key Laboratory of Physical Chemistry of Solid Surfaces.

Appendix A. Supplementary data

Supplementary data associated with this article can be found, in the online version, at <https://doi.org/10.1016/j.apcatb.2019.04.022>.

References

- [1] M.K. Debe, *Nature* 486 (2012) 43.
- [2] Z.W. Seh, J. Kibsgaard, C.F. Dickens, I.B. Chorkendorff, J.K. Nørskov, T.F. Jaramillo, *Science* 355 (2017) 6321.
- [3] V.K. Puthiyapara, D.J.L. Brett, A.E. Russell, W.F. Lin, C. Hardacre, *ACS Appl. Mater. Interfaces* 8 (2016) 12859.
- [4] L. Adamczyk, J.A. Cox, K. Miecznikowski, *Int. J. Hydrogen Energy* 42 (2017) 5035.
- [5] P.J. Barczuk, K. Miecznikowski, P.J. Kulesza, *J. Electroanal. Chem.* 600 (2007) 80.
- [6] K. Miecznikowski, P.J. Kulesza, *J. Power Sources* 196 (2011) 2595.
- [7] K. Miecznikowski, *Arab. J. Chem.* (2016), <https://doi.org/10.1016/j.ijhydene.2016.11.011>.
- [8] H.H. Li, Q.Q. Fu, L. Xu, S.Y. Ma, Y.R. Zheng, X.J. Liu, S.H. Yu, *Energy Environ. Sci.* 10 (2017) 1751.
- [9] Z.M. Cao, Q.L. Chen, J.W. Zhang, H.Q. Li, Y.Q. Jiang, S.Y. Shen, G. Fu, B.A. Lu, Z.X. Xie, L.S. Zheng, *Nat. Commun.* 8 (2017) 15131.
- [10] X.K. Gu, B. Liu, J. Greeley, *ACS Catal.* 5 (2015) 2623.
- [11] J. Schnaidt, M. Heinen, Z. Jusys, R.J. Behm, *J. Phys. Chem. C* 116 (2013) 2872.

- [12] J.S. Spendelov, A. Wieckowski, *Phys. Chem. Chem. Phys.* 9 (2007) 2654.
- [13] Y. Hoshi, T. Yoshida, A. Nishikata, T. Tsuru, *Electrochim. Acta* 56 (2011) 9011.
- [14] L. Dubau, M. Lopez-Haro, L. Castanheira, J. Durst, M. Chatenet, P. Bayle-Guillemaud, L. Guetaz, N. Caque, E. Rossinot, F. Maillard, *Appl. Catal. B: Environ.* 142 (2013) 801.
- [15] A.K. Schuppert, A. Savan, A. Ludwig, K.J.J. Mayrhofer, *Electrochim. Acta* 144 (2014) 332.
- [16] Z.N. Yu, Z. Zhang, Z.-S. Lv, M.-T. Liu, L. Zhang, A.-J. Wang, L.-Y. Jiang, J.-J. Feng, J. Colloid Interface Sci. 525 (2018) 216.
- [17] Y.-C. Shi, J.-J. Feng, X.-X. Lin, L. Zhang, J.H. Yuan, Q.-L. Zhang, A.-J. Wang, *Electrochim. Acta* 293 (2019) 504.
- [18] X.-Y. Huang, A.-J. Wang, X.-F. Zhang, L. Zhang, J.-J. Feng, *ACS Appl. Energy Mater.* 1 (2018) 5779.
- [19] X.L. Xu, X. Zhang, H. Sun, Y. Yang, X.P. Dai, J.S. Gao, X.Y. Li, P.F. Zhang, H.H. Wang, N.F. Yu, S.G. Sun, *Angew. Chem. Int. Ed.* 53 (2014) 12522.
- [20] N. Tian, Z.Y. Zhou, S.G. Sun, Y. Ding, Z.L. Wang, *Science* 316 (2007) 732.
- [21] M.F. Li, Z.P. Zhao, T. Cheng, A. Fortunelli, C.Y. Chen, R. Yu, Q.H. Zhang, L. Gu, B.V. Merinov, Z.Y. Lin, E.B. Zhu, T. Yu, Q.Y. Jia, J.H. Guo, L. Zhang, W.A. Goddard, Y. Huang, X.F. Duan, *Science* 354 (2016) 1414.
- [22] S.C.S. Lai, N.P. Lebedeva, T.H.M. Housmans, M.T.M. Koper, *Top. Catal.* 46 (2007) 320.
- [23] L. Cao, T. Mueller, *Nano Lett.* 16 (2016) 7748.
- [24] Y.T. Pan, L.Q. Yan, Y.T. Shao, J.M. Zuo, H. Yang, *Nano Lett.* 16 (2016) 7988.
- [25] J. Erlebacher, M.J. Aziz, A. Karma, N. Dimitrov, K. Sieradzki, *Nature* 410 (2001) 450.
- [26] Z.Q. Niu, N. Becknell, Y. Yu, D. Kim, C. Chen, N. Kornienko, G.A. Somorjai, P.D. Yang, *Nat. Mater.* 1 (2016) 1188.
- [27] V.A. Bogdanovskaya, M.R. Tarasevich, *Russ. J. Electrochem.* 47 (2011) 380.
- [28] Y. Li, F. Quan, L. Chen, W. Zhang, H. Yu, C. Chen, *RSC Adv.* 4 (2014) 1895.
- [29] C. Zhang, W. Sandorf, Z. Peng, *ACS Catal.* 5 (2015) 2296.
- [30] X.Q. Huang, Z.P. Zhao, L. Cao, Y. Chen, E.B. Zhu, Z.Y. Lin, M.F. Li, A.M. Yan, A. Zettl, Y.M. Wang, X.F. Duan, T. Mueller, Y. Huang, *Science* 348 (2015) 1230.
- [31] B. Vera, G. Martin, W. Elena, R. Stefan, H. Marc, E.D. Rafal, W. Marc-Georg, S. Peter, *Nano Lett.* 16 (2016) 1719.
- [32] B.-A. Lu, T. Sheng, N. Tian, Z.-C. Zhang, C. Xiao, Z.-M. Cao, H.-B. Ma, Z.-Y. Zhou, S.-G. Sun, *Nano Energy* 33 (2017) 65.
- [33] L. Chen, L. Lu, H. Zhu, Y. Chen, Y. Huang, Y. Li, L. Wang, *Nat. Commun.* 8 (2017) 14136.
- [34] S. Wang, L. Xiong, J. Bi, X. Zhang, G. Yang, S. Yang, *ACS Appl. Mater. Interfaces* 10 (2018) 27009.
- [35] N. Jung, S. Bhattacharjee, S. Gautam, H. Park, J. Ryu, Y.H. Chung, S.Y. Lee, I. Jang, J.H. Jang, S.H. Park, D.Y. Chung, Y.E. Sung, K.H. Chae, U.V. Waghmare, S.C. Lee, S.J. Yoo, *NPG Asia Mater.* 8 (2016) 237.
- [36] H.X. Liu, N. Tian, M.P. Brandon, J. Pei, Z.C. Huangfu, C. Zhan, Z.Y. Zhou, C. Hardacre, W.F. Lin, S.-G. Sun, *Phys. Chem. Chem. Phys.* 14 (2012) 16415.
- [37] Y. Wang, H.Y. Zhuo, H. Sun, X. Zhang, X.P. Dai, C.L. Luan, C.L. Qin, H.H. Zhao, J. Li, M.L. Wang, J.Y. Ye, S.-G. Sun, *ACS Catal.* 9 (2019) 442.
- [38] Z.C. Zhang, J.F. Hui, Z.C. Liu, X. Zhang, J. Zhuang, X. Wang, *Langmuir* 28 (2012) 14845.
- [39] B. Delley, *J. Chem. Phys.* 92 (1990) 508.
- [40] B. Delley, *J. Chem. Phys.* 113 (2000) 7756.
- [41] S. Kurth, J.P. Perdew, P. Blaha, *Int. J. Quantum Chem.* 75 (1999) 889.
- [42] J.P. Perdew, K. Burke, M. Ernzerhof, *Phys. Rev. Lett.* 77 (1996) 3865.
- [43] T.A. Halgren, W.N. Lipscomb, *Chem. Phys. Lett.* 49 (1977) 225.
- [44] Y. Wang, H.Y. Zhuo, X. Zhang, X.P. Dai, K.M. Yu, C.L. Luan, L. Yu, Y. Xiao, J. Li, M.L. Wang, F. Gao, *Nano Energy* 48 (2018) 590.
- [45] C.Z. Li, Q. Yuan, B. Ni, T. He, S.M. Zhang, Y. Long, L. Gu, X. Wang, *Nat. Commun.* 9 (2018) 3702.
- [46] W.P. Xiao, M.A.L. Cordeiro, M.X. Gong, L.L. Han, J. Wang, C. Bian, J. Zhu, H.L. Xin, D.L. Wang, *J. Mater. Chem. A* 5 (2017) 9867.
- [47] S.T. Hunt, M. Milina, Z. Wang, Y. Roman-Leshkov, *Energ. Environ. Sci.* 9 (2016) 3290.
- [48] V. Crist, BE Lookup Table for Signals from Elements and Common Chemical Species. Handbook of Monochromatic XPS Spectra, The Elements of Native Oxides, Kamiasao Asao-Ku, Kawasaki, Japan 1999.
- [49] C. Li, T. Liu, T. He, B. Ni, Q. Yuan, X. Wang, *Nanoscale* 10 (2018) 4670.
- [50] Y. Wang, G.W. Wang, G.W. Li, B. Huang, J. Pan, Q. Liu, J.J. Han, L. Xiao, J.T. Lu, L. Zhuang, *Energy Environ. Sci.* 8 (2015) 177.
- [51] N.L. Yang, Z.C. Zhang, B. Chen, Y. Huang, J.Z. Chen, Z.C. Lai, Y. Chen, M. Sindoro, A.L. Wang, H.F. Cheng, Z.X. Fan, X.Z. Liu, B. Li, Y. Zong, L. Gu, H. Zhang, *Adv. Mater.* 29 (2017) 1700769.
- [52] Y.P. Zuo, D.W. Rao, S. Li, T.T. Li, G.L. Zhu, S.M. Chen, L. Song, Y. Chai, H.Y. Han, *Adv. Mater.* 30 (2018) 1704171.
- [53] K.Z. Jiang, P.T. Wang, S.J. Guo, X. Zhang, X. Shen, G. Lu, D. Su, X.Q. Huang, *Angew. Chem. Int. Ed.* 55 (2016) 9030.
- [54] H. Liu, Y. Zheng, G.X. Wang, S.Z. Qiao, *Adv. Energy Mater.* 5 (2015) 618.
- [55] Y.G. Suo, L. Zhuang, J.T. Lu, *Angew. Chem. Int. Ed.* 46 (2007) 2862.
- [56] J.B. Wu, P.P. Li, Y.T. Pan, S. Warren, X. Yin, H. Yang, *Chem. Soc. Rev.* 41 (2012) 8066–8074.
- [57] V.R. Stamenkovic, B.S. Mun, M. Arenz, K.J.J. Mayrhofer, C.A. Lucas, G.F. Wang, P.N. Ross, N.M. Markovic, *Nat. Mater.* 6 (2007) 241.
- [58] T.Y. Liu, K. Wang, Q. Yuan, Z.B. Shen, Y. Wang, Q.H. Zhang, X. Wang, *Nanoscale* 9 (2017) 2963.
- [59] L. Zhang, S.I. Choi, J. Tao, H.C. Peng, S.F. Xie, Y.M. Zhu, Z.X. Xie, Y.N. Xia, *Adv. Funct. Mater.* 24 (2014) 7520.
- [60] Y.L. Zheng, S.L. Zhao, S.L. Liu, H.H. Yin, Y.Y. Chen, J.C. Bao, M. Han, Z.H. Dai, *ACS Appl. Mater. Interfaces* 7 (2015) 5347.
- [61] D.F. van der Vliet, C. Wang, D.G. Li, A.P. Paulikas, J. Greeley, R.B. Rankin, D. Strmcnik, D. Tripkovic, N.M. Markovic, V.R. Stamenkovic, *Angew. Chem. Int. Ed.* 51 (2012) 3139.
- [62] A.A. Siller-Ceniceros, M.E. Sanchez-Castro, D. Morales-Acosta, J.R. Torres-Lubian, E. Martinez, F.J. Rodriguez-Varela, *Appl. Catal. B: Environ.* 209 (2017) 455.
- [63] L. Zhuang, J. Jin, H.D. Abruna, *J. Am. Chem. Soc.* 129 (2007) 11033.
- [64] D.J. Chen, Y.Y.J. Tong, *Angew. Chem. Int. Ed.* 54 (2015) 9394.
- [65] Z.M. Cui, H. Chen, M.T. Zhao, D. Marshall, Y.C. Yu, H. Abruna, F.J. DiSalvo, *J. Am. Chem. Soc.* 136 (2014) 10206.
- [66] L. Bai, *Appl. Surf. Sci.* 433 (2018) 279.
- [67] N. Zhang, Y.M. Zhu, Q. Shao, X. Zhu, X.Q. Huang, *J. Mater. Chem. A* 5 (2017) 18977.
- [68] Y.G. Feng, L.Z. Bu, S.J. Guo, J. Guo, X.Q. Huang, *Small* 12 (2016) 4464.
- [69] L. Liu, X.X. Lin, S.Y. Zou, A.J. Wang, J.R. Chen, J.J. Feng, *Electrochim. Acta* 187 (2016) 576.
- [70] F. Colmati, G. Tremiliosi, E.R. Gonzalez, A. Berna, E. Herrero, J.M. Feliu, *Phys. Chem. Chem. Phys.* 11 (2009) 9114.
- [71] V. Del Colle, A. Berna, G. Tremiliosi, E. Herrero, J.M. Feliu, *Phys. Chem. Chem. Phys.* 10 (2008) 3766.
- [72] V. Del Colle, J. Souza-Garcia, G. Tremiliosi, E. Herrero, J.M. Feliu, *Phys. Chem. Chem. Phys.* 13 (2011) 12163.
- [73] P.A. Christensen, A. Hamnett, *J. Electroanal. Chem.* 260 (1989) 347.
- [74] L. Demarconnay, S. Brimaud, C. Coutanceau, J.M. Leger, *J. Electroanal. Chem.* 601 (2007) 169.
- [75] Y.Y. Yang, J. Ren, H.X. Zhang, Z.Y. Zhou, S.G. Sun, W.B. Cai, *Langmuir* 29 (2013) 1709–1710.
- [76] G. Socrates, *Infrared Characteristic Group Frequencies*, Wiley, New York, 1966.
- [77] J. Schnaidt, M. Heinen, Z. Jusys, R.J. Behm, *J. Phys. Chem. C* 116 (2012) 2872.
- [78] J. Schnaidt, M. Heinen, Z. Jusys, R.J. Behm, *Catal. Today* 202 (2013) 154.
- [79] S.C. Chang, Y. Ho, M.J. Weaver, *J. Am. Chem. Soc.* 113 (1991) 9506.
- [80] L.Q. Wang, H. Meng, P.K. Shen, C. Bianchini, F. Vizza, Z.D. Wei, *Phys. Chem. Chem. Phys.* 13 (2011) 2667.
- [81] Y.Y. Yang, J. Ren, Q.X. Li, Z.Y. Zhou, S.G. Sun, W.B. Cai, *ACS Catal.* 4 (2014) 798.
- [82] B. Wieland, J.P. Lancaster, C.S. Hoaglund, P. Holota, W.J. Tornquist, *Langmuir* 12 (1996) 2594.
- [83] N.P. Lebedeva, A. Rodes, J.M. Feliu, M.T.M. Koper, R.A. van Santen, *J. Phys. Chem. B* 106 (2002) 9863.
- [84] I.J. McPherson, P.A. Ash, L. Jones, A. Varambhia, R.M.J. Jacobs, K.A. Vincent, *J. Phys. Chem. C* 121 (2017) 17176.
- [85] S.S. Laletina, M. Mamatkulov, E.A. Shor, V.V. Kaichev, A. Genest, I.V. Yudanov, N. Rosch, *J. Phys. Chem. C* 121 (2017) 17371.
- [86] F.P. Kong, C.Y. Du, J.Y. Ye, G.Y. Chen, L. Du, G.P. Yin, *ACS Catal.* 7 (2017) 7923.
- [87] M. Vandichel, A. Moscu, H. Gronbeck, *ACS Catal.* 7 (2017) 7431.
- [88] M.J. Lee, J.S. Kang, Y.S. Kang, D.Y. Chung, H. Shin, C.Y. Ahn, S. Park, M.J. Kim, S. Kim, K.S. Lee, Y.E. Sung, *ACS Catal.* 6 (2016) 2398.
- [89] Z.C. Zhang, Z.M. Luo, B. Chen, C. Wei, L. Zhao, J.Z. Chen, X. Zhang, Z.C. Lai, Z.X. Fan, C.L. Tan, M.T. Zhao, Q.P. Lu, B. Li, Y. Zong, C.C. Yan, G.X. Wang, Z.J.C. Xu, H. Zhang, *Adv. Mater.* 28 (2016) 8712.
- [90] W.Y. Zhao, B. Ni, Q. Yuan, P.L. He, Y. Gong, L. Gu, X. Wang, *Adv. Energy Mater.* 7 (2017) 1601593.
- [91] N. Zhang, X.Y. Li, H.C. Ye, S.M. Chen, H.X. Ju, D.B. Liu, Y. Lin, W. Ye, C.M. Wang, Q. Xu, J.F. Zhu, L. Song, J. Jiang, Y.J. Xiong, *J. Am. Chem. Soc.* 138 (2016) 8928.
- [92] G.R. Xu, B. Wang, J.Y. Zhu, F.Y. Liu, Y. Chen, J.H. Zeng, J.X. Jiang, Z.H. Liu, Y.W. Tang, J.M. Lee, *ACS Catal.* 6 (2016) 5260.